Review

CO$_2$ reforming of CH$_4$ over Co–La-based perovskite-type catalyst precursors

Gustavo Valderrama [a,*], Caribay Urbina de Navarro [b], Mireya R. Goldwasser [c]

[a] Laboratorio de Catálisis, Petróleo y Petroquímica, Unidad de Estudios Básicos, Universidad de Oriente – Núcleo Bolívar, La Sabanita, Calle San Simón, Estado Bolívar 8001, Venezuela
[b] Centro de Microscopía Electrónica, Facultad de Ciencias, Universidad Central de Venezuela, Paseo los Ilustres, Los Chaguaramos, Caracas 1040, Venezuela
[c] Centro de Catálisis, Petróleo y Petroquímica, Escuela de Química – Universidad Central de Venezuela, Paseo los Ilustres, Los Chaguaramos, Caracas 1040, Venezuela

HIGHLIGHTS

► The precursors solids La$_{1-x}$Sr$_x$CoO$_3$ were synthesized by the auto combustion method.
► XRD *in situ* confirmed the thermal stability and transformations of the perovskite.
► Co^0 nanoparticles highly dispersed in La$_2$O$_2$CO$_3$–SrO are obtained by reduction process.
► The interaction between CO$_2$ and La$_2$O$_3$ produces La$_2$O$_2$CO$_3$ phase.
► The catalysts inhibit carbon formation despite the severe reaction conditions.

ARTICLE INFO

ABSTRACT

A series of perovskite-type oxides based on La–Sr–Co (La$_{1-x}$Sr$_x$CoO$_3$) were synthesized by the auto combustion method and used as precursors for the catalytic methane dry reforming (MDR) at 1073 K, atmospheric pressure under continuous flow of reactant gases with a CH$_4$:CO$_2$ = 1:1 ratio. Catalysts were characterized by techniques such as X-ray diffraction (XRD), BET specific surface area, temperature-programmed reduction-oxidation (TPR–TPO) and scanning-transmission electron microscopy (SEM–TEM). Formation of La–Sr–Co–O solid solutions was confirmed by the more intense diffraction peaks and cell parameter measurements. It was observed that the activation/reduction process occurs through intermediary species producing Co^0 nano-size particles over the SrO and La$_2$O$_3$ phases, which are highly dispersed in the La$_2$O$_2$CO$_3$–SrO solid matrix responsible for the high activity and low carbon formation despite the severe reaction conditions used. The presence of Sr in doping quantities slightly promotes secondary reactions such as carbon formation and water–gas shift retarding partially the dry reforming reaction.

1. Introduction

The burnout of the world crude oil reserves will unchain some international conflicts on account of the natural resources access mainly of fossil origin; this situation will originate a serious economic crisis at world especially in the countries without technologies replaceable toward the energy generation. Similarly, the imminent danger of global warming partly caused by greenhouse gas emission from burning fossil fuels has driven both the scientific and industrial communities to search for environment-friendly energy sources [1]. This scenario suggests as an energetic strategy, a radical change of the vector energetic petroleum-based to an econom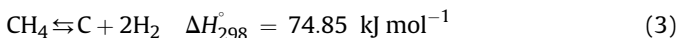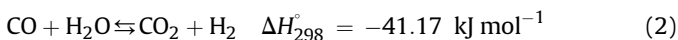y hydrogen-based which is the more efficient, clean and sure energy source considered. This situation convert natural gas (methane) as the excellent raw material for hydrogen production due to the existence of immense reserves at world level, high H/C ratio, less CO$_2$ emitted by unit of energy produced during its combustion, among others. In this sense, new technologies are required to efficiently transform natural gas to fuel and/or products chemicals that replace those coming from the petroleum [2].

Among natural gas reforming processes, the dry reforming of methane with CO$_2$ has recently increased interest because of the lower H$_2$/CO ratios produced (Eq. (1)) sometimes lower than unity due to the simultaneous occurrence of the reverse water–gas shift reaction (RWGS, Eq. (2)) that can be used industrially as raw material for the Fischer–Tropsch synthesis [3] and to valuable oxygenated chemicals (such as aldehydes, methanol, dimethyl ether, acetic acid, etc., and to unsaturated hydrocarbons) [4]. In addition, the dry reforming allows using natural gas reserves containing considerable quantities of CO$_2$, contributing to transform these

* Corresponding author. Tel.: +58 285 6329296; fax: +58 285 6321271.
E-mail addresses: vgustavo@udo.edu.ve, vfgustavo@yahoo.com (G. Valderrama).

greenhouse gases (CO_2 and methane). However, due to the fact that this reaction presents a high thermodynamic potential ($\Delta G_{298} = 174.6$ kJ mol^{-1}), it requires the use of high temperatures to revert its spontaneity (for example $\Delta G_{1073} = -44.76$ kJ mol^{-1}), condition which promotes simultaneously carbon formation (Eq. (3)) leading to catalysts deactivation.

$$CH_4 + CO_2 \leftrightarrows 2CO + 2H_2 \quad \Delta H^{\circ}_{298} = 247 \text{ kJ mol}^{-1} \quad (1)$$

$$CO + H_2O \leftrightarrows CO_2 + H_2 \quad \Delta H^{\circ}_{298} = -41.17 \text{ kJ mol}^{-1} \quad (2)$$

$$CH_4 \leftrightarrows C + 2H_2 \quad \Delta H^{\circ}_{298} = 74.85 \text{ kJ mol}^{-1} \quad (3)$$

Noble metal-based catalysts used in the reforming of CH_4 [5], are less sensitive to coking, contrary to Fe, Co and Ni based catalysts that show high activity but are rapidly deactivated [6]. However, the high cost of noble metals and their limited availability promote the development of Co and Ni-based catalytic systems that inhibit coke formation. As it has been shown [7], coke formation decreases with downsizing metallic particle on the support. An alternative is to use metal-based precursors with a well-defined structure, as perovskite-type oxides (ABO_3) which produce metallic particles in the order of nanometers under reducing atmosphere [8] diminishing coke formation and increasing the activity of the catalysts. Other advantage of perovskite-type oxides is its redox properties, due to the fact that a wide range of elements can be incorporated in the structure by partial substitution of A and/or B cations, giving rise to a combination of elements with different oxidation states [9].

In previous work we reported the physicochemical properties and the behavior of $La_{1-x}Sr_xNiO_3$ and $La_{2-2x}Sr_{2x}NiO_{4-\delta}$ as catalyst precursors in dry reforming of methane [10], which show high activity and resistance to coke deposition [11]. Recently we reported that ternary solid solutions $LaNi_{1-x}Co_xO_3$ [12] and quaternary $La_{1-x}Sr_xNi_{1-y}Co_yO_3$ [13] show high metallic dispersion and produces a synergetic effect between these particles to inhibit coke formation. The aim of the present work is to investigate the use of perovskite-type solid solutions $La_{1-x}Sr_xCoO_3$ as precursors of highly dispersed Co nanoparticles to avoid coke formation during the dry reforming of methane under continuous flow of reactive gases. We also investigated the possible carbon nanotubes formation.

2. Experimental

2.1. Synthesis of perovskite-type oxides

The ternary perovskite-type $La_{1-x}Sr_xCoO_3$ were synthesized by the auto combustion method [14], which consist of adding glycine ($H_2NCH_2CO_2H$) to an aqueous solution of metallic nitrates [$La(NO_3)_3 \bullet 6H_2O$, $Co(NO_3)_2 \bullet 6H_2O$, $Sr(NO_3)_2$] to obtain a $NO_3^-/NH_3 = 1$ M ratio. The resulting solution is formed by dissolving the salts in their own occluded water at ~ 323 K with constant stirring. The solvent is then slowly evaporated at ~ 373 K until a resin is formed. The glycine acts as metal complexing agent and as a pyrophoric substance. The increase of the heating temperature up to ~ 523 K producing a spontaneous exothermic reaction (auto combustion) that allows the formation of the precursor powder which is then calcined in air (973–1173 K, 2 h) to remove any carbon residue.

2.2. Characterization

The solids were characterized by means of techniques such as X-ray diffraction (XRD), BET surface area, temperature-programmed reduction and oxidation (TPR–TPO) and scanning-transmission electron microscopy (SEM–TEM).

The *ex situ* XRD analysis were conducted in a Siemens D500 diffractometer with Cu K$_\alpha$ radiation ($\lambda = 1.5418$ Å, 40 kV, 30 mA). The acquisition of the data were performed according to the required study; e.g. the scanning of the angular zone from 10° to 90° 2θ (0.05 2θ step, 27 s) were used to obtain the initials phases and cell parameters, and the angular zone between 32° and 35° 2θ (0.02 2θ step, 30 s) was used to confirm the solid solution formation. Samples were prepared by the powder chamber method, which consists of finely crushing the solid (0.05–0.1 g) to ensure a homogeneous and abundant size of the grain, and placed on the sample holder and irradiated with X-rays. The *in situ* XRD analyses were performed to study the effect of degassing and of the reduction temperature on the crystal structure; the finely crushed sample on methanol was placed on a platinum plate. Heating was conducted increasing the temperature at 4 K min^{-1} from room temperature to 1173 K under Ar or H_2 atmospheres according to the analysis to be performed. The diffractograms were recorded at different temperatures every 50 K in order to determine the temperature at which phases transformations occur. Phase's recognition was obtained by comparison with JCPDS files using the database PDF2 and software EVA 3.30 programs. The particle size diameter was calculated by the Scherrer equation using the more intense diffraction peaks [15].

The specific surface areas were determined by N_2 adsorption at 77 K, using 0.1–0.2 g of sample previously out gassed at 623 K for 2 h, with a $N_2/Ar = 30/70$ ratio on a Micromeritics Flow Sorb II. The TPR experiments were carried out in a quartz reactor loaded with 0.05 g of the solid. Pulses of hydrogen (12 µmol H_2) were injected every 2 min while the temperature was risen from room to 1173 K at 4 K min^{-1}. The TPR experiments were followed by temperature programmed oxidation (TPO) in order to study the reversibility of the reduction. After cooling to room temperature, the reduced sample was exposed to He diluted O_2 pulses. The temperature program was similar to that described for TPR experiments. Prior to redox cycles, samples were heated at 873 K for 2 h under Ar.

The morphological and elemental analyses were performed by means of a SEM S-500 microscope coupled to energy dispersive X-ray (EDX) at 20 kV and 3.1×10^{-9} A, on samples covered with Au or C respectively. Metal dispersion after reduction and carbon

Table 1
Chemical analysis, phases and textural properties of $La_{1-x}Sr_xCoO_3$ solids.

| Stoichiometry		Tcalc. (K)	SA$_{BET}$ (m^2 g^{-1})	XRD phases (as-synthesized)	Particle size (nm)	XRD phases (after TPR/TPO)	XRD phases (after catalytic test)
(Nominal)	(Experimental)						
$LaCoO_3$	$La_{0.99}CoO_3$	973	5	$LaCoO_3$	19	$LaCoO_3$	Co, La_2O_3
$La_{0.9}Sr_{0.1}CoO_3$	$La_{0.89}Sr_{0.06}CoO_3$	973	8	$La_{0.9}Sr_{0.1}CoO_3$	19	$La_{0.9}Sr_{0.1}CoO_3$	
$La_{0.8}Sr_{0.2}CoO_3$	$La_{0.76}Sr_{0.13}CoO_3$	973	12	$La_{0.8}Sr_{0.2}CoO_{3-x}$	19	$La_{0.9}Sr_{0.1}CoO_3$	Co,
		1073	10		20		$La_2O_2CO_3$
		1173	5		21		SrO
$La_{0.7}Sr_{0.3}CoO_3$	$La_{0.68}Sr_{0.21}CoO_3$	1073	14	$La_{0.6}Sr_{0.4}CoO_3$	18	$La_{0.8}Sr_{0.2}CoO_{3-x}$	
$La_{0.6}Sr_{0.4}CoO_3$	$La_{0.63}Sr_{0.22}CoO_3$	1073	18	$La_{0.6}Sr_{0.4}CoO_3$	17	$La_{0.6}Sr_{0.4}CoO_3$	
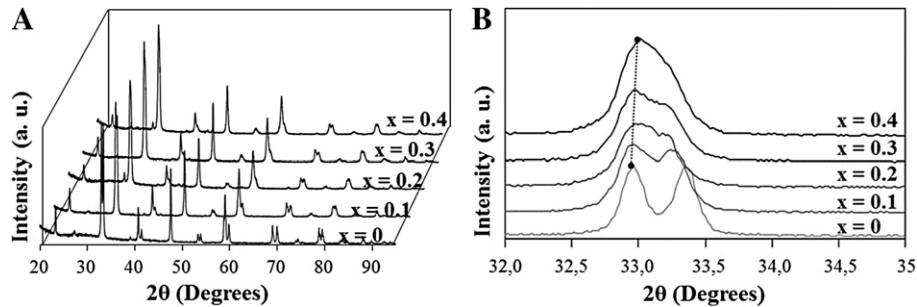
Fig. 1. XRD patterns of La$_{1-x}$Sr$_x$CoO$_3$ system (A) and of more intense peaks (B).

deposition on the catalyst after reaction were studied by TEM with an H-500 microscope. The samples were placed in an ethanol–water solution and dispersed by ultrasonic, a drop was placed on a metal grid with collodion and allowed to dry, before introducing into the microscope chamber.

2.3. Dry reforming of methane

The activity tests were performed using 0.05 g of the catalyst diluted in 0.15 g of sea sand (to maintain the bed temperature constant) in a 20-mm ID tubular quartz reactor at 1073 K and atmospheric pressure operated in a fixed-bed continuous flow system with CH$_4$:CO$_2$ = 1:1 ratio, diluted in Ar (80%) to make the mixture less explosive and a space velocity WHSV = 24 L g$_{cat}^{-1}$ h^{-1}. Before catalytic tests, the solids were reduced *ex situ* in H$_2$ (reducing conditions: 20 mL min^{-1}, 1073 K, 5 h). After reduction, the reactor was placed in the reaction system and adjusted to the reaction temperature. The water produced during reaction, was condensed before passing the reactants and products to the analyzing system, which consisted of an on-line gas chromatograph (Perkin Elmer Auto System XL) equipped with an automatic injection, a thermal conductivity detector and provided with a Carbosieve SII 80/100 (12′ × 1/8′ OD SS) column.

The CH$_4$ and CO$_2$ conversions are defined as the CH$_4$ and CO$_2$ converted per total amount of CH$_4$ and CO$_2$ fed, respectively. The selectivity to CO was calculated based on carbon balance and defined as $S_{CO}(\%) = (\eta_{CO}/[\eta_{CH_4(c)} + \eta_{CO_2(c)}])*100$; while hydrogen selectivity was calculated as $S_{H_2}(\%) = (\eta_{H_2}/[2*\eta_{CH_4(c)}])*100$, where η_{CO} and η_{H_2} are the moles of CO and hydrogen produced and $\eta_{CH_4(c)}$ and $\eta_{CO_2(c)}$ are the amounts of methane and carbon dioxide converted, as describe elsewhere [11].

3. Results and discussion

The main characteristics of the catalysts are summarized in Table 1. XRD results confirm the advantages of the auto-combustion method [16], since it produces solids of crystalline phases with perovskite-type structures at low calcined temperatures and high purity as suggested by the absence of other phases in XRD patterns (Fig. 1A). The elemental analyses show a good correlation between experimental and the nominal composition, with BET surface areas

between 5 and 18 m^2 g^{-1} in agreement with previously reported values [11–13] and particle sizes in the range of 17–21 nm (Table 1).

Amplification of the angular signal between 32° and 35° (2θ scale) corresponding to the more the intense diffraction peaks of La$_{1-x}$Sr$_x$CoO$_3$ (Fig. 1B), show a doubly degenerated signal characteristic of the rhombohedra symmetry [17]. The increase of the amount of Sr in the perovskite, overlap both signals giving rise to an asymmetric wide peak, characteristic of a distorted rhombohedra structure. Additionally, a linear tendency between the peaks is observed with the increase of Sr (Fig. 1B), suggesting the formation of a La–Sr–Co–O solid solution [13], this hypothesis is confirmed by calculating the cell parameters of the crystalline phases presented in (Table 2).

To investigate the effect of the partial substitution of A cations on the rhombohedra cell parameters, these were calculated for each value of Sr content (x), indexing the two most intensive diffraction signals (Fig. 1A) in the crystallographic planes ($h\ k\ l$) corresponding to (1 1 0) and (0 2 4) of LaCoO$_3$ phase (JCPDS 25-1060) to a hexagonal system, since the distorted rhombohedra symmetry is similar to that of an ideal hexagonal symmetry. The rhombohedra parameters obtained are shown in (Table 2). Hexagonal and rhombohedra symmetries were calculated by the following equations:

Hexagonal symmetry: $a = b \neq c$, $\alpha = \beta = 90°$ $\gamma = 120°$

$$\text{Sen}^2\,\theta = \left(\lambda^2/3a^2\right)*\left(h^2 + k^2 + hk\right) + \left(\lambda^2 l^2/4ac^2\right) \quad (4)$$

$$1/4d^2 = \left(1/3a^2\right)*\left(h^2 + k^2 + hk\right) + \left(l^2/4c^2\right) \quad (5)$$

Rhombohedra symmetry: $a = b = c$, $\alpha = \beta = \gamma \neq 90°$

$$a_R^2 = \left(a_{HEX}^2/3\right) + \left(c_{HEX}^2/9\right) \quad (6)$$

Table 2
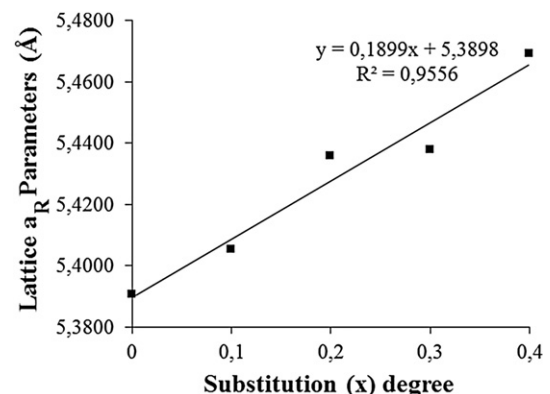Cell parameters of hexagonal and rhombohedra symmetries of La$_{1-x}$Sr$_x$CoO$_3$ solids.

Precursor solid	Hexagonal symmetry			Rhombohedra symmetry	
	a (Å)	b (Å)	c (Å)	a (Å)	Angle (degrees)
LaCoO$_3$	5.4350	5.4350	13.1496	5.3906	60.54
La$_{0.9}$Sr$_{0.1}$CoO$_3$	5.4350	5.4350	13.2044	5.4054	60.36
La$_{0.8}$Sr$_{0.2}$CoO$_3$	5.4350	5.4350	13.3160	5.4358	59.99
La$_{0.7}$Sr$_{0.3}$CoO$_3$	5.4254	5.4254	13.3353	5.4379	59.85
La$_{0.6}$Sr$_{0.4}$CoO$_3$	5.4254	5.4254	13.4503	5.4693	59.47

Fig. 2. Rhombohedra a_R cell parameters of La$_{1-x}$Sr$_x$CoO$_3$ systems.
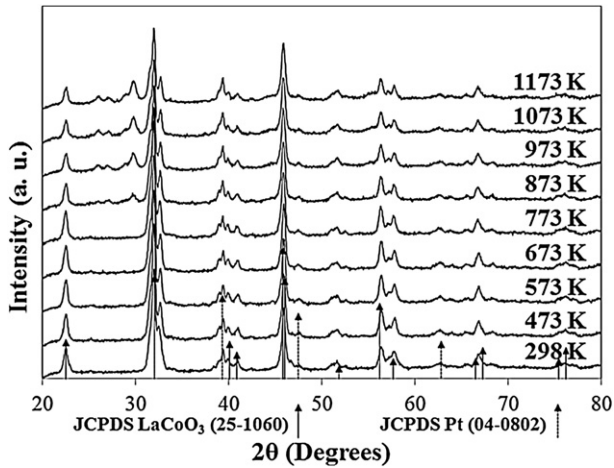
Fig. 3. LaCoO$_3$: *in situ* XRD patterns as a function of temperature on Ar during the degassing process. Dotted lines correspond to the Pt sample holder.

$$\text{Sen}\,(\alpha/2) = 3 \Big/ \left(2\sqrt{\left(3 + (c_{HEX}/a_{HEX})^2\right)}\right) \tag{7}$$

As expected the La$_{1-x}$Sr$_x$CoO$_3$ cell rhombohedra parameters increase with Sr content from 5.3906 to 5.4693 Å (Fig. 2), since the substitution of La^{3+} with a 1.36 Å radium by Sr^{2+} with a larger radium 1.44 Å, causes an increase of the d_{A-O} distance in the perovskite structure. The calculated rhombohedra cell parameters (Table 2) follow Vegart Law [18] that defines solid solutions, that is to say, they show a lineal variation with respect to the Sr substitution degree (x) (Fig. 2), confirming formation of solid solutions by these systems.

The increase of the calcined temperature causes a decrease of the surface area and an increase of the particle size (Table 1), due to sintering promoted by exposing the solid to high temperatures. According to the *in situ* XRD patterns of LaCoO$_3$ (Fig. 3) during the degassing process at various temperatures (298−1173 K) under argon atmosphere, the perovskite-type structure of LaCoO$_3$ is maintained even under the severe thermal conditions used, confirming the high stability shown by this type of structure [19,20].
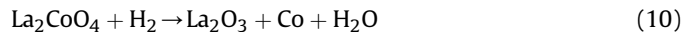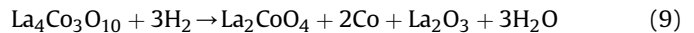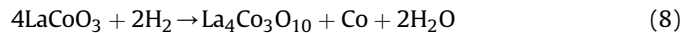
In order to obtain information of the behavior of La$_{1-x}$Sr$_x$CoO$_3$ under reductive atmosphere, TPR studies were performed by injecting a series of hydrogen pulses (Fig. 4A). The sample was heated under argon at 873 K prior to the reduction reaction. Three hydrogen consumption peaks can be observed (Table 3), indicating the presence of Co species with different particle size and the formation of oxygen deficient intermediates, which can also be corroborated by the *in situ* XRD analysis of LaCoO$_3$ under H$_2$ atmosphere at different

Table 3
Temperatures and percentage of reduction and particle size of La$_{1-x}$Sr$_x$CoO$_3$ solids.

Precursor solid	1st peak (R)		2nd peak (R)		3rd peak (R)		Total	*Particle size Co^0	
	T (K)	Red (%)	T (K)	Red (%)	T (K)	Red (%)	Red (%)	(nm)^a	(nm)^b
LaCoO$_3$	723	25.4	898	21.5	1065	34.9	82	23	15
La$_{0.9}$Sr$_{0.1}$CoO$_3$	718	23.8	883	12.5	1073	48.4	85	25	
La$_{0.8}$Sr$_{0.2}$CoO$_3$	733	24.5	893	14.0	1073	44.5	83	22	12
La$_{0.7}$Sr$_{0.3}$CoO$_3$	735	25.0	898	14.8	1093	46.4	86	22	
La$_{0.6}$Sr$_{0.4}$CoO$_3$	767	26.0	893	14.4	1097	47.5	88	22	10

*C^0 metal particle size calculated from: ^{a}Scherrer equation, ^{b}MET.

temperatures (Fig. 4B). Formation of La$_4$Co$_3$O$_{10}$ phase was observed at 723 K without total destruction of the LaCoO$_3$ perovskite-type phase (Fig. 4B); corroborating the lattice oxygen mobility [20]. La$_2$CoO$_4$ spinel-type phase was formed at 873 K consistent with that reported by Nakamura et al. [19]. Total reduction to metallic Co and La$_2$O$_3$ takes place at 1073 K (Fig. 4B) [21]. When comparing the reduction temperatures we assume that these phases correspond to the three reduction peaks of LaCoO$_3$ (Fig. 4A), respectively. According to those results the step reduction reactions can be suggested as:

$$4LaCoO_3 + 2H_2 \rightarrow La_4Co_3O_{10} + Co + 2H_2O \tag{8}$$

$$La_4Co_3O_{10} + 3H_2 \rightarrow La_2CoO_4 + 2Co + La_2O_3 + 3H_2O \tag{9}$$

$$La_2CoO_4 + H_2 \rightarrow La_2O_3 + Co + H_2O \tag{10}$$

Since similar reduction profiles were observed for all solids (Fig. 4A), the reduction behavior of LaCoO$_3$ (Eqs. (8)−(10)) can be extrapolated to Sr doped solids, where total reduction generate Co^0, La$_2$O$_3$ and SrO [13]. However, it is observed that the total reduction occur to lightly higher temperatures as the degree of substitution by Sr increases. The similarity of the reduction profiles (Fig. 4A) suggests that Sr do not exert a noticeable effect on the process, since the reduction depend mainly on the nature of the transition metal (Co). However, the presence of Sr slightly increases the percentage of reduction (Table 3). Considering the case where trivalent La^{3+} cations in LaCoO$_3$ are partially replaced by divalent Sr^{2+} cations, the charge compensation can be achieved by the stoichiometric formation of either tetravalent Co^{4+} (or positive holes) or oxide ion vacancies La$_{1-x}$Sr$_x$CoO$_{3-\lambda}$ [22]. Concerning the electronic effects, a simple charge balance calculation indicates that, assuming oxidation states +3, +2 and −2 for La, Sr and O, respectively, the formal oxidation state of Co decreases from 3+ ($x = 0$) to 2.6+ ($x = 0.4$), corroborating the fact that the presence of Sr promotes electrons dopant effect which favor reduction of the solid.
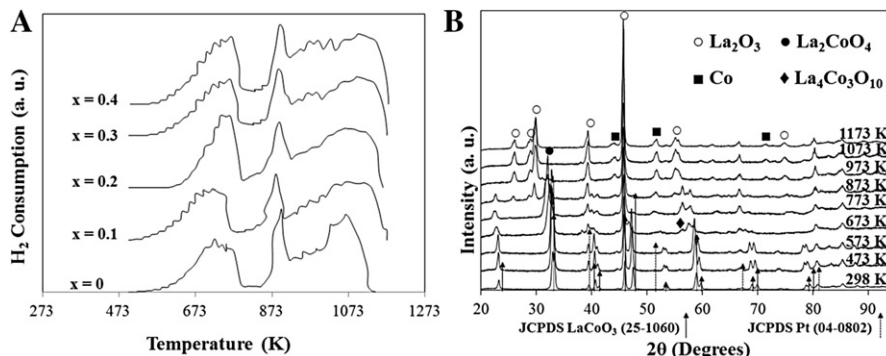

Fig. 4. (A) TPR profiles of La$_{1-x}$Sr$_x$CoO$_3$ and (B) LaCoO$_3$ crystalline phases as a function of the reduction temperature. The dotted lines correspond to the Pt sample holder.
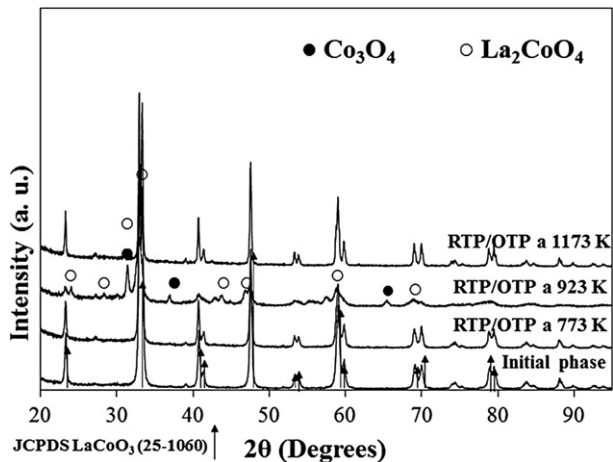
Fig. 5. *Ex situ* XRD patterns of LaCoO3 subjected to three redox cycles (TPR followed by TPO) at different temperatures.

Table 4
Methane dry reforming results over $La_{1-x}Sr_xCoO_3$.

x	$\%X_{CH_4}$	$\%X_{CO_2}$	$\%S_{H_2}$	$\%S_{CO}$	η_{CO}/η_{H_2}
0	93.6	98.9	89.1	93.7	1.05
0.1	86.0	91.0	80.2	88.6	1.11
0.2	64.5	74.1	83.7	99.9	1.29
0.3	53.5	73.8	80.5	98.7	1.23
0.4	61.4	79.0	88.6	99.9	1.17

$T_{reac.}$: 1073 K; $t_{reac.}$: 30 h; $CH_4:CO_2 = 1:1$; Ar (80%).
WHSV = 24 L g_{cat}^{-1} h^{-1}; (x): Sr substitution degree.

A series of three redox cycles (TPR followed by TPO) at different temperatures was performed on the perovskite-type oxide LaCoO3 to determine the reversibility of the redox processes. The XRD pattern obtained after the first redox cycle at 773 K (Fig. 5) shows that LaCoO3 perovskite-type structure is preserved, confirming the ability of the structure to release/accept oxygen in the lattice during the redox process. The second redox cycle at 923 K destroys the perovskite structure and produces a mixture of Co_3O_4 and La_2CoO_4 oxides (Fig. 5). However, the LaCoO3 perovskite-type structure is restored by subjecting the sample to a third redox cycle at 1173 K (Fig. 5, Table 1), these results suggest that the redox processes

reversibly occurs on LaCoO3 solid, because the formation of the perovskite-type structure is thermodynamically favored at higher temperatures compare to formation of Co mixed oxides [23]. Such redox reversibility can be extrapolated to all Sr-doped solids since they showed the same reduction profile (Fig. 4A), demonstrated by the XRD phases after TPR/TPO (Table 1).

The morphological analyses of calcined $La_{1-x}Sr_xCoO_3$ solids ($x = 0$, 0.2, 0.4) (Fig. 6), show macro-pores formation due to the release of large quantities of gases such as NO_x, CO_x and $H_2O_{(v)}$ resulting from the auto-combustion of the gel formed by glycine and nitrates [14]. As the degree of Sr substitution (x) increases in $La_{1-x}Sr_xCoO_3$ the macro-porosity slightly increases (Fig. 6), suggesting that the auto-combustion process is more exothermic and therefore flue gases are violently released to the atmosphere. The elemental analyses (SEM–EDX) in specific zones of the randomly selected sample (high zoom) and the total sample (low zoom), show high homogeneity in composition due to solid solutions formed by these systems.

TEM micrographs of $La_{1-x}Sr_xCoO_3$ reduced solids with $x = 0$, 0.2, 0.4 (Fig. 7) show high dispersion of the metallic Co particles that clearly differ from the matrix solid composed of La_2O_3 and SrO
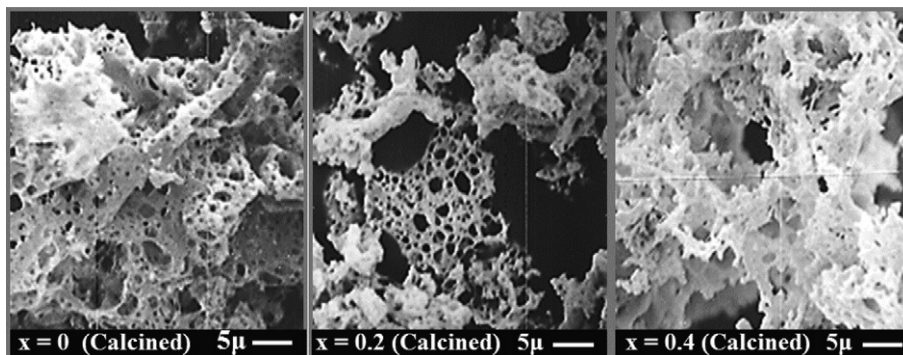

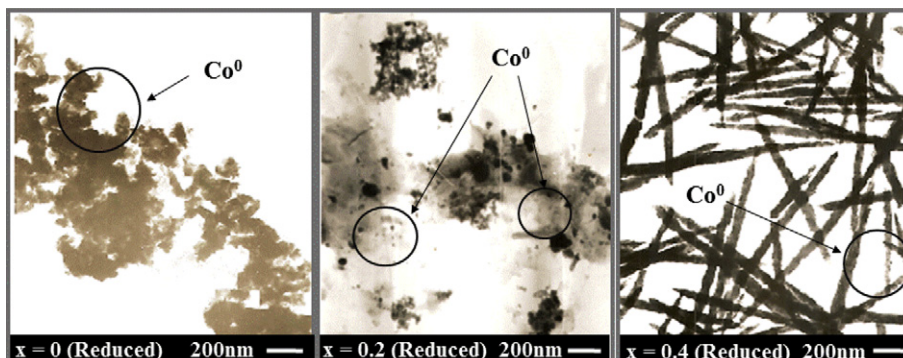Fig. 6. SEM micrographs of calcined solids $La_{1-x}Sr_xCoO_3$ ($x = 0$, 0.2, 0.4).

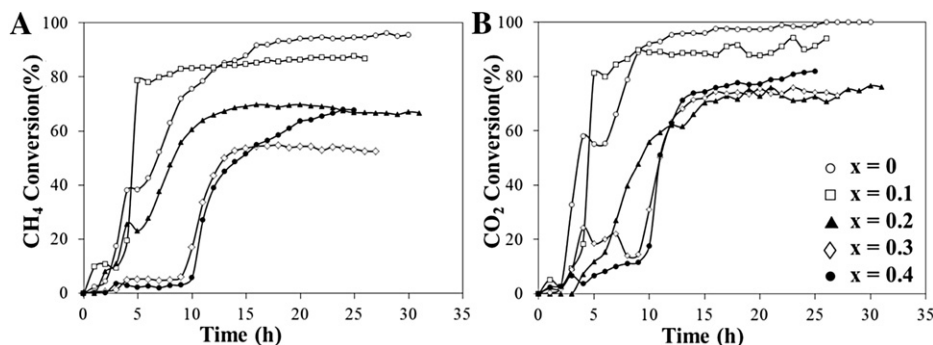Fig. 7. TEM micrographs of reduced solids $La_{1-x}Sr_xCoO_3$ ($x = 0$, 0.2, 0.4).

Fig. 8. Conversions obtained in the dry reforming under continuous flow over La$_{1-x}$Sr$_x$CoO$_3$ at 1073 K. CH$_4$ (A) and CO$_2$ (B).
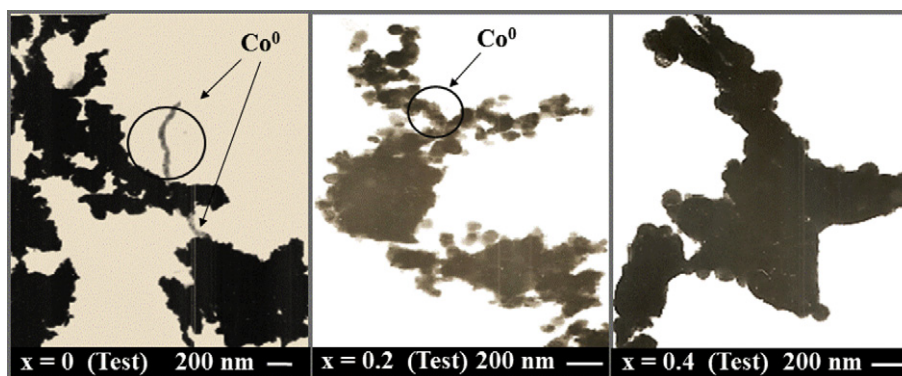

Fig. 9. TEM images of solids La$_{1-x}$Sr$_x$CoO$_3$ ($x = 0$, 0.2, 0.4) after test catalytic at 1073 K.

oxides, formed during the reduction process [13]. Particle size are in the order of 10–15 nm (some isolated Co particles are identified in the circle, Fig. 7), similar to those determine by the Scherrer equation, which decreases slightly with increasing Sr content (Table 3). These results corroborate the advantages of using perovskite-type oxides as precursor catalysts since after reduction, they produce highly disperse metallic particles.

Table 4 summarizes the catalytic parameters obtained in the methane dry reforming at 1073 K on La$_{1-x}$Sr$_x$CoO$_3$ reduced solids. It is observed that the highest activity is shown by LaCoO$_3$ with CO$_2$ and CH$_4$ conversions of 93.6 and 98.9% respectively (Table 4) that remain constant for ~30 h (Fig. 8). Moreover, the increase of the substitution degree (x) decreases the conversion (Table 4) and requires an induction time to activate the solid, e.g. $x = 0.4$ had ~10 h of induction time to be active for the reaction, note that the doped solids with strontium shows a tendency to increase the conversions after 30 h of reaction (Fig. 8). This behavior is due to the fact that Sr doped solids need slightly higher temperatures during reduction to form the active species (Co^0) compared with the un-doped solid (Fig. 4A).

For the Sr doped solids, CH$_4$ conversions were slightly smaller than CO$_2$ conversions (Fig. 8A). These results indicate that the presence of Sr slightly favors the reverse water–gas shift reaction (RWGS Eq. (2)) giving rise to larger CO$_2$ conversions (Fig. 8B) and higher selectivity to CO, increasing η_{CO}/η_{H2} molar ratio (Table 4).

XRD (Table 1) and TEM analyses (Fig. 9) of solids after catalytic tests, revealed the presence of Co, SrO and La$_2$O$_2$CO$_3$ phases. The presence of SrCO$_3$ phase formed in CO$_2$ atmosphere has been reported [11]; however it was not detected in our work. The presence of SrCO$_3$ phase with a very small particle size could difficult its detection by XRD. Similarly it could be formed as a reaction intermediate which we propose play a very important role in the dry

reforming reaction, contributing to formation of La$_2$O$_2$CO$_3$ and SrO regeneration [13]. TEM micrographs of solids with $x = 0$, 0.2 and 0.4 (Fig. 9), show carbon nanotubes formation in very small quantities despite the severe reaction conditions used ($T = 1073$ K and time of ~30 h), these nanotubes are constituted of small, well dispersed Co metallic particles (Fig. 9). The incorporation of Sr produces a dopant electron effect which stabilizes Co^0 metallic particles, furthermore the Co nanosize particles (Table 3) and their high dispersion in the (La$_2$O$_2$CO$_3$–SrO) matrix of the solid contributes to maintain high activity and inhibit carbon formation of the catalysts during the dry reforming of methane.

4. Conclusions

The XRD analysis indicates that the sol–gel method via auto-combustion was appropriate for the synthesis of La–Sr–Co–O perovskite-type solid solutions with high degree of purity, crystalline and thermal stability. The redox processes on the solids shown to be reversible with the oxygen of LaCoO$_3$ perovskite-type oxide shown certain mobility. TPR analysis showed that the presence of doping quantities of Sr induce reduction of solids at slightly higher temperatures with formation of Co^0 metallic phase, in the order of nanometers, highly dispersed on the reduced matrix formed by La$_2$O$_3$ and SrO phases. The interaction between CO$_2$ and La$_2$O$_3$ produces La$_2$O$_2$CO$_3$ phase.

The stabilization of the cobalt metallic particles by the doping electronic effect caused by Sr, the small nanosize particles and its high dispersion in the matrix of the solid (La$_2$O$_2$CO$_3$–SrO), play a very important role in the dry reforming of methane, inhibiting carbon formation, despite the severe reaction conditions used, giving rise to highly active and stable catalysts.

Acknowledgments

Appendix A. Supplementary data

Supplementary data related to this article can be found at http://dx.doi.org/10.1016/j.jpowsour.2013.01.142.

References

[1] P. Voser, Energy Strategy Rev. 1 (2012) 3–4.
[2] L.S. Neiva, L. Gama, Braz. J. Pet. Gas 4 (3) (2010) 119–127.
[3] K. Koo, J. Yoon, H. Kim, J. Yang, H. Joo, Res. Chem. Intermed. 34 (8–9) (2008) 803–810.
[4] S. Minteer, Alcoholic Fuels, CRC Press: Taylor & Francis Group, 6000 Broken Sound Parkway NW, Suite 300. Boca Raton, FL 33487-2742, 2006.
[5] M.A. Gerber, Review of Novel Catalysts for Biomass Tar Cracking and Methane Reforming, Pacific Northwest National Laboratory Operated by Battelle for the U.S. Department of Energy under Contract DE-AC05-76RL01830, Richland, Washington 99354, 2007, Online: http://www.ntis.gov/ordering.htm.
[6] J. Guo, H. Lou, Y. Zhu, X. Zheng, Mater. Lett. 57 (2003) 4450–4455.
[7] A.T. Bell, Science 299 (2003) 1688–1691.
[8] B. Echchahed, S. Kaliaguine, H. Alamdari, Int. J. Chem. React. Eng. 4 (2006) A29.
[9] J.L.G. Fierro, Metal Oxides: Chemistry and Applications, CRC Press: Taylor & Francis Group, 6000 Broken Sound Parkway NW, Suite 300. Boca Raton, FL 33487-2742, 2006.
[10] G. Valderrama, M.R. Goldwasser, E. Pietri, M.J. Pérez-Zurita, M.L. Cubeiro, C. Urbina de Navarro, Interciencia 30 (6) (2005) 332–338.
[11] G. Valderrama, M.R. Goldwasser, C. Urbina de Navarro, J.M. Tatibouët, J. Barrault, C. Batiot-Duperyrat, F. Martínez, Catal. Today 107–108 (2005) 785–791.
[12] G. Valderrama, A. Kiennemann, M.R. Goldwasser, Catal. Today 133–135 (2008) 142–148.
[13] G. Valderrama, A. Kiennemann, M.R. Goldwasser, J. Power Sources 195 (2010) 1765–1771.
[14] L.A. Chick, L.R. Pederson, G.D. Maupin, J.L. Bates, L.E. Thomas, G.J. Exharos, Mater. Lett. 10 (1–2) (1990) 6–12.
[15] H.P. Klug, L.E. Alexander, X-ray Diffraction Procedure for Polycrystalline and Amorphous Materials, second ed., Wiley-Interscience Publication, New York, 1974.
[16] J. Guo, H. Lou, Y. Zhu, X. Zheng, J. Nat. Gas Chem. 12 (1) (2003) 17–22.
[17] L.G. Tejuca, J.L.G. Fierro, J.M.D. Tascon, Adv. Catal. 36 (1998) 237–328.
[18] M. Stojanovic, R.G. Haverkamp, C.A. Mims, H. Moudallal, A. Jacobson, J. Catal. 166 (2) (1997) 315–323.
[19] T. Nakamura, G. Petzow, L. Gauckler, Mater. Res. Bull. 14 (5) (1979) 649–659.
[20] Y.L. Lee, J. Kleis, J. Rossmeisl, D. Morgan, Phys. Rev. B 80 (224101) (2009) 1–20.
[21] F. Martínez, C. Batiot-Dupeyrat, G. Valderrama, J.M. Tatibouët, C. R. Acad. Sci. II C 4 (1) (2001) 49–55.
[22] R.J.H. Voorhoeve, D. Johnson, J. Remeika, P. Gallagher, Science 195 (1977) 827–833.
[23] O.M. Sreedharan, M.S. Chandrasekharaiah, J. Mater. Sci. 21 (1986) 2581–2584.